Available online at www.sciencedirect.com
SCIENCE DIRECT®
Journal of Power Sources 118 (2003) 35–43
JOURNAL OF POWER SOURCES
www.elsevier.com/locate/jpowsour

Stability of Fe–Cr alloy interconnects under CH_4–H_2O atmosphere for SOFCs

Teruhisa Horita*, Yueping Xiong, Katsuhiko Yamaji, Natsuko Sakai, Harumi Yokokawa

National Institute of Advanced Industrial Science and Technology (AIST), Higashi 1-1-1, Tsukuba, Ibaraki 305-8565, Japan

Abstract

The chemical stability of Fe–Cr alloys (ZMG232 and SUS430) was examined under humidified CH_4 gases at 1073 K to simulate the real anode atmosphere in SOFC operation. Surface microstructure change and oxide scale layer formation were observed on the oxidized Fe–Cr alloy surfaces. The main reaction products were Mn–Cr–(Fe) spinels for both alloys. Secondary ion mass spectrometry (SIMS) was applied to measure the elemental distribution of minor and major elements around the oxide scale/alloy interface. A high concentration of Mn on the oxide scale surface suggested the fast diffusion of Mn in the oxide scale to form the spinels. Annealing in CH_4–H_2O made the oxide scale thicker with duration time on the alloy surface. The parabolic growth rates (k_p) of oxide scale layer were evaluated from the thickness of oxide scales by secondary ion mass spectrometry (SIMS) depth profiles, which were calculated to the following: $k_p = 6.25 \times 10^{-6}$ μm^2/s for SUS430 and $k_p = 4.42 \times 10^{-6}$ μm^2/s for ZMG232. The electrical conductivity of oxidized alloys showed the semi-conductor temperature dependence for both alloys. The electrical conductivity of oxidized ZMG232 alloy was higher than that of oxidized SUS430.

Keywords: Fe–Cr alloy; Solid oxide fuel cells (SOFCs); Interconnects; Oxide scales

1. Introduction

Solid oxide fuel cells (SOFCs) are one of the promising high-energy conversion systems that produce electricity and heat. The development of SOFCs is now coming to the second generation. That is, the second generation SOFCs operates at a temperature around 873–1073 K with an internal reforming of hydrocarbon fuels. With a reduction of operation temperature, alloy materials can be applied to interconnect of SOFCs. Merits of applying alloys to the interconnects in SOFCs are: (1) achievement of dense and gas-tightness between fuel and air gases, (2) easy for handling, which makes cheaper fabrication cost, and (3) high electronic and thermal conductivity, which makes the cell performance higher. On the other hand, under operation at high temperatures, oxide scale formation occurs on the alloy surface with reacting the atmospheric gases, such as O_2, H_2O, CO, CO_2, and CH_4.

So far, several kinds of alloys are examined as candidates for interconnect in medium operation temperature SOFCs [1–18]. Because Cr_2O_3 forming alloys show relatively low electrical resistance (high resistance against oxidation), these materials are attractive and suitable for interconnect applications. Among the Cr_2O_3 forming alloys, ferritic steel containing some active elements can form relatively stable oxide scale and reduce the Cr vaporization [12–18]. Thus, the ferristic alloys are promising materials for the interconnect SOFCs in medium temperature operation [17,18]. The oxidation mechanism and oxide scale formation of ferritic alloys have been reported by several groups, especially in air and H_2–H_2O atmosphere [12–19]. On the other hand, there still remain uncertainly about oxidation of alloy and oxide scale formation in CH_4 or reforming gas atmospheres.

The aims of this study are to investigate the chemical stability of ferritic alloys against the oxidation in anode atmospheres, especially in CH_4–H_2O atmospheres to simulate anode atmospheres. Two different kinds of Fe–Cr alloys (ZMG232 and SUS430) were selected for testing in CH_4–H_2O atmospheres. Elemental distribution was analyzed by SIMS to detect minor and major elements in depth direction precisely.

2. Experimental

2.1. Materials

Commercially available Fe–Cr alloys were examined for oxidation experiments; one is multi-purpose commercially

* Corresponding author. Tel.: +81-298-61-4540; fax: +81-298-61-4540.
E-mail address: t.horita@aist.go.jp (T. Horita).

0378-7753/03/$ – see front matter © 2003 Elsevier Science B.V. All rights reserved.
doi:10.1016/S0378-7753(03)00058-2

Table 1
Chemical composition of Fe–Cr alloy examined for oxidation analysis

Element	Mass	
	ZMG232 (Hitachi Metals Ltd., Japan)	SUS430
C	0.02	0.048
Si	0.40	0.35
Mn	0.50	0.21
Ni	0.26	0.12
Cr	21.97	16.31
Al	0.21	0.11
Zr	0.22	0.023
La	0.04	0.0006
Fe	76.38	82.8

available alloy, SUS430 and the other is specially developed alloy for SOFC interconnect, ZMG232 (supplied from Hitachi Metals Ltd.). The chemical compositions of these alloys are listed in Table 1. These alloys contain Fe and Cr with several kinds of minor elements; C, Si, Mn, Ni, Al, La, and Zr. The stability of ZMG232 alloy has already been examined in O_2 atmosphere [17]. The electrical conductivity of this alloy was only 6 mΩ cm^2 at 1273 K after operation at 1273 K for 1000 h [17]. The surface of the alloys was polished with a diamond paste up to 0.25 μm finish to obtain a clean and flat surface.

2.2. Oxidation experiments (CH_4–H_2O treatments)

The alloys were annealed at 1073 K under CH_4–Ar mixture with saturation of H_2O. A mixture of CH_4 and Ar was passed through H_2O (at 50 °C) in a flow rate of 50 ml/min. The mixed gases have the following partial pressure of each gas before feeding to the reactor tube: $p(CH_4) = 0.11$ bar, $p(Ar) = 0.79$ bar and $p(H_2O) = 0.10$ bar. The oxidation treatments were examined at 1073 K for 3–792 h in an Al_2O_3-tube reactor. When the mixed gases were supplied to the reactor at 1073 K, the CH_4–H_2O gas should be converted to the following composition assuming that the equilibrium is attained in the reactor: $p(O_2) = 5.23 \times 10^{-23}$ bar, $p(H_2) = 2.57 \times 10^{-1}$ bar, $p(H_2O) = 2.85 \times 10^{-3}$ bar, $p(CO) = 8.40 \times 10^{-2}$ bar, $p(CO_2) = 1.01 \times 10^{-3}$ bar, $p(CH_4) = 3.25 \times 10^{-3}$ bar. In this gas composition, the equilibrium calculation suggests that carbon deposition will occur. The experimental observation confirmed the deposition of carbon inside the Al_2O_3-tube reactors.

2.3. Analysis of alloys

Surface microstructure was analyzed by scanning electron microscope (SEM, Hitachi S-800) with EDX (Kevex). The reaction phases formed on the alloy surface were identified by X-ray diffraction (XRD) (Phillips PW 1800). In order to analyze the microstructure of oxide scales at the interfaces, the cross-section of the oxide scale/alloy interface was observed by SEM. Major and minor elements distributions were analyzed by SIMS (CAMECA, ims-5f) in its depth profile mode. The primary O_2^+ beam sputtered the sample surface, and M^+ secondary ions were collected as a function of sputtering time (depth from surface) in the area of 150–250 μm^2 (M: each metal species, acceleration voltage: 10 kV, primary beam intensity: 50–100 nA). For observing the distribution of light elements (such as hydrogen, carbon, oxygen, and sulfur), the primary Cs^+ beam was adopted to sputter the sample surface, and signal counts of $^1H^-$, $^{12}C^-$, $^{16}O^-$, and $^{32}S^-$ were measured as a function of depth from the surface.

The electrical conductivity of oxidized alloy was measured by two-probe ac impedance measurements [16]. Pt-paste electrodes were applied to the surface of the oxidized alloy surfaces, and the measurements were conducted in air atmosphere.

3. Results and discussion

3.1. Surface microstructure and formed phases

Fig. 1 shows microstructures of oxidized alloy surfaces in CH_4–H_2O atmosphere at 1073 K for 72 h. The microstructures of the alloy surface is varied drastically by the CH_4–H_2O atmosphere; the grain boundary parts increase in height (Fig. 1a and c) and needle- or plate-like grains are observed on the alloy surface (Fig. 1b and d). On the ZMG232 surface, the grain boundaries are plate-like shape grains and the other parts are cubic shape grains (Fig. 1b). On the other hand, on the SUS430 surface, whole surface of oxidized alloy is covered with plate-like grains (Fig. 1d). The microstructures of oxidized alloys are observed for prolonged annealing duration time. Fig. 2 shows microstructures of oxidized alloys annealed at 1073 K for 144 h in CH_4–H_2O. On the ZMG232 surface, plate-like grains and cubic-shape grains cover the whole surface of alloy. For SUS430 surface, whole surface is covered with plate-like grains, which is different from the case of ZMG232. For both surfaces, distinct grain boundaries are not observed, which suggests thick oxide scale layer formation on the alloy surface. Fig. 3 shows oxidized alloy surface annealed at 1073 K for 1032 h in CH_4–H_2O. Many cubic-shape grains cover the ZMG232 surface (Fig. 3a) and these cubic shape grains consist of porous structure on the top surface of oxide scale. For the oxidized SUS430 surface, many needle-like grains cover the whole surface of alloy. The microstructures of the oxide scale are significantly different from each other.

To confirm the phases formed in the oxide scale, XRD analysis was examined for the oxide scale. Figs. 4 and 5 show XRD patterns of oxidized alloy surface for different annealing duration times. The identified phases in the oxidized alloys are Mn–Cr–(Fe) spinel oxides (marked as S in the patterns), Cr_2O_3 oxides (marked as C in the patterns), and

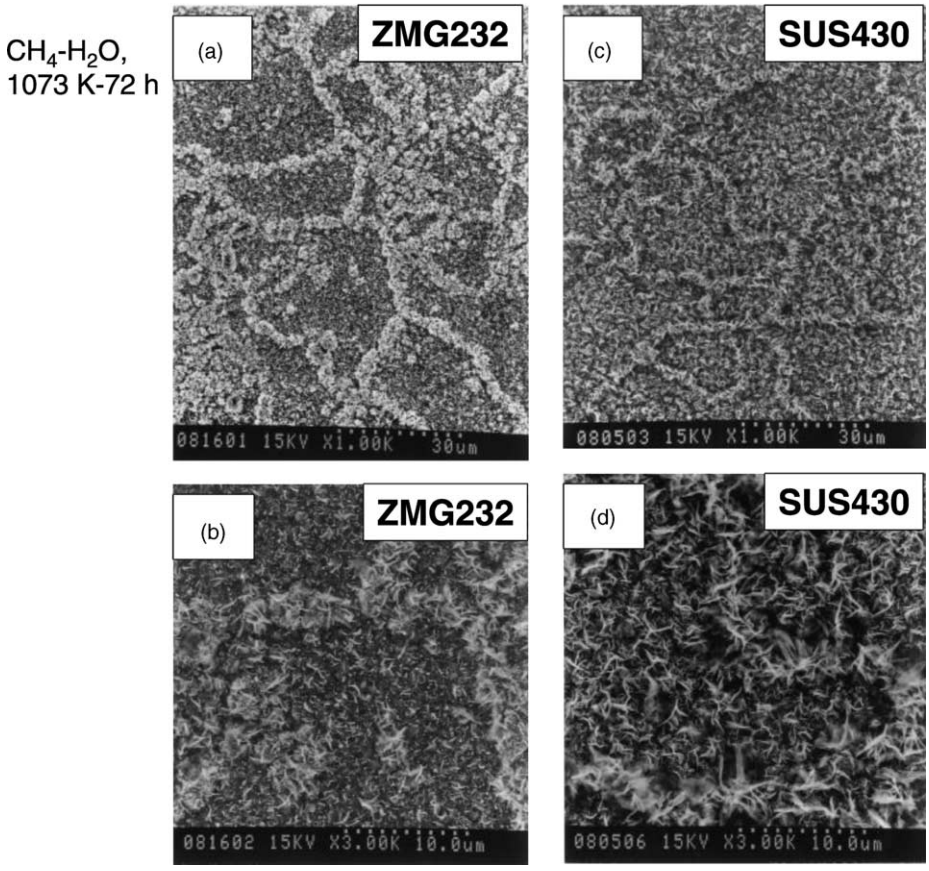

Fig. 1. Scanning microscope images of oxidized alloy surface (oxidation at 1073 K for 72 h in CH_4–H_2O atmosphere): (a) ZMG232 alloy surface, (b) high magnification of ZMG232 alloy surface, (c) SUS430 alloy surface, (d) high magnification of SUS430 alloy surface.

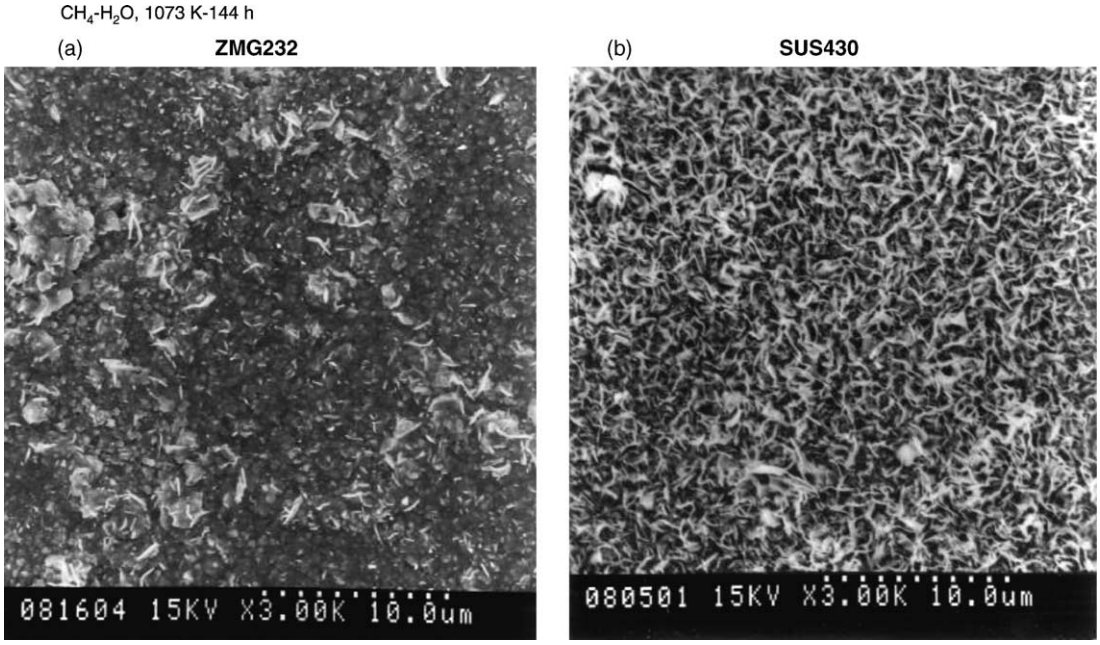

Fig. 2. Scanning microscope images of oxidized alloy surface (oxidation at 1073 K for 144 h in CH_4–H_2O atmosphere): (a) ZMG232 alloy surface, (b) SUS430 alloy surface.

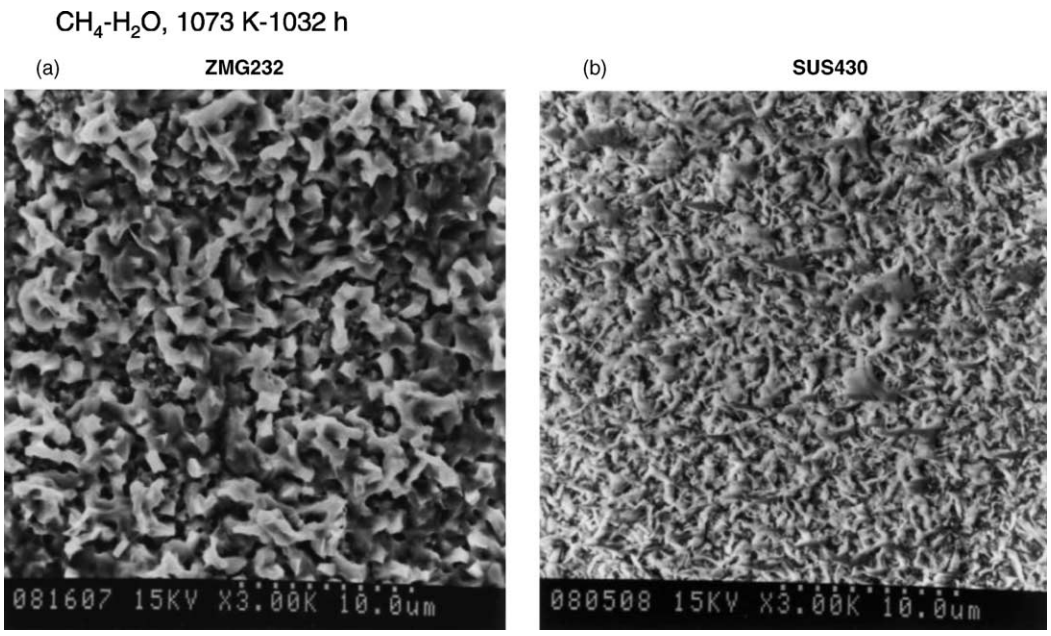

Fig. 3. Scanning microscope images of oxidized alloy surface (oxidation at 1073 K for 1032 h in CH_4–H_2O atmosphere): (a) ZMG232 alloy surface, (b) SUS430 alloy surface.

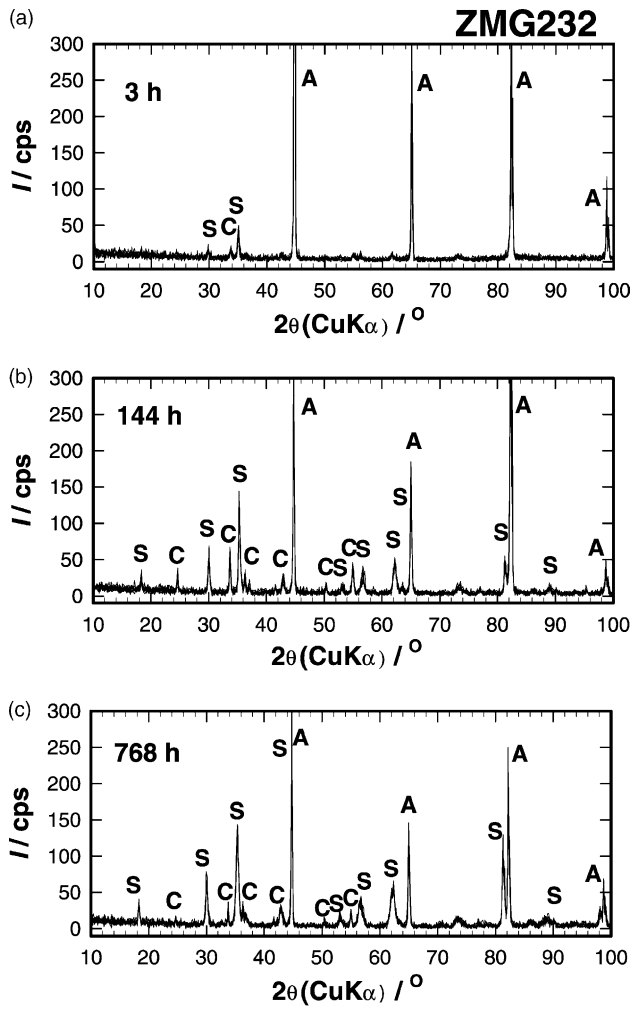

Fig. 4. X-ray diffraction patterns of oxidized ZMG232 alloy surface in CH_4–H_2O atmosphere: (a) 3 h, (b) 144 h, (c) 768 h.

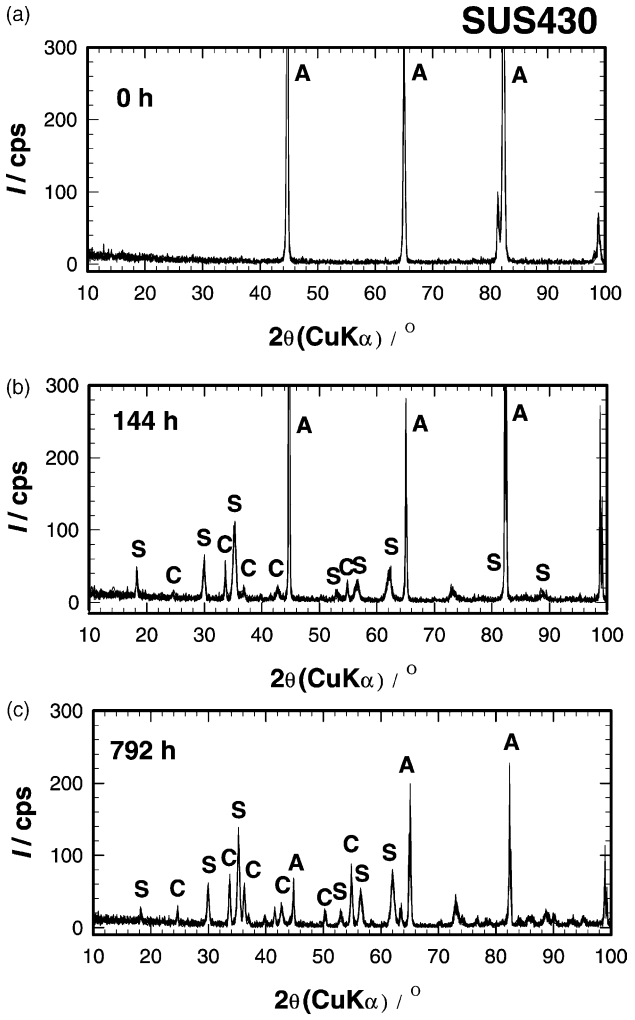

Fig. 5. X-ray diffraction patterns of oxidized SUS430 alloy surface in CH_4–H_2O atmosphere: (a) 3 h, (b) 144 h, (c) 768 h.

alloy themselves (marked as A in the patterns). With increasing the oxidation duration times, the peaks intensities attributed to spinel oxides become higher, which suggests the formation of thick reaction products on the surface. Similar phases are observed for ZMG232 alloy and SUS430 alloy. This suggests that the formed oxides on the surface are similar in the crystal structure between these two alloys. For XRD peaks attributed to spinel phases, some peak shifts are observed between these alloys. This indicates the minor crystal structure change in the spinel phases in oxide scales. Minor crystal structure change can be attributed to the minor elements in the oxide scale.

3.2. Microstructures of cross-section at the oxide scale/alloy interfaces

Fig. 6 shows microstructures of cross-section at the oxide scale/alloy interfaces for ZMG232 and SUS430. Thick and dense oxide scales formed on the alloys surface for both cases. The oxide scale/alloy interfaces are clear without any voids and cracks for both alloys. Therefore, the oxide scale grew continuously on alloy by diffusion process.

In Fig. 6a, oxide scale is identified as dark zone on the ZMG232 alloy surface with a thick and dense microstructure. Many dark spots are observed inside the alloy; these spots are Al_2O_3-rich parts from EDX analysis and these are inner oxides of Al_2O_3. The Al_2O_3 inner oxides are observed in the oxidized ZMG232 alloy in H_2–H_2O atmosphere [19].

In Fig. 6b, the microstructure of the oxide scale layer in SUS430 is somewhat different from that in ZMG232. A relatively thick oxide scale grew on the alloy surface. Also, no inner Al_2O_3 spots are observed in the alloy. This microstructure of SUS430 is completely different from that of ZMG232. Although Al_2O_3 inner oxides are observed in the SUS430 annealed in air atmosphere, no such spots are observed in the samples annealed in CH_4–H_2O. This may be related to the concentration of Al and phase stability of Al_2O_3 in the annealed atmosphere.

3.3. SIMS depth profiles

Fig. 7 shows SIMS depth profiles of composed elements around the oxide scale/alloy interface. In Fig. 7a, SIMS signal counts of oxidized ZMG232 are shown as a function of depth from the surface. High concentration of Cr, Mn, and Fe are observed in the oxide scale, which suggests the formation of Mn–Cr–Fe oxides on the surface. This result supports the XRD patterns and SEM/EDX observation that the Mn–Cr–Fe spinels are observed on the surface. For minor elements, high concentration of La is observed in the oxide scale, whereas the counts of Zr are low in the oxide scale but high in the alloy. The oxide scale thickness is considered to be about 1200 nm from the profile of Cr^+.

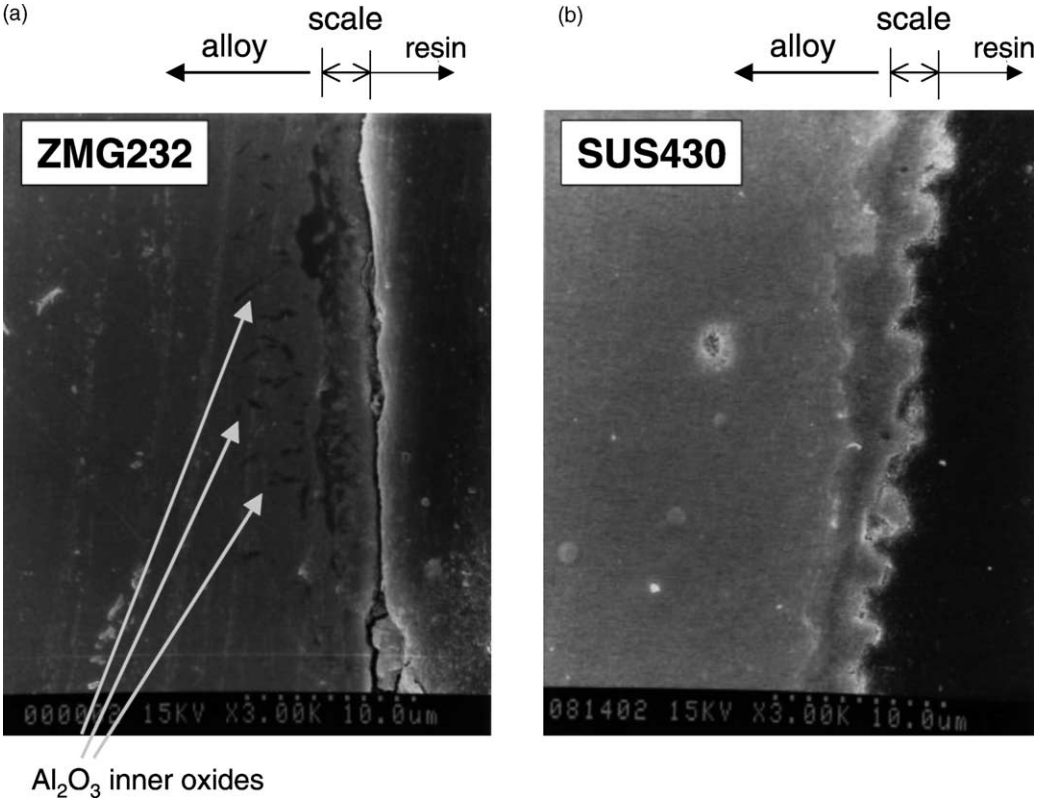

Fig. 6. Microstructures of cross-sections at the oxide scale/alloy interfaces annealed at 1073 K for 1032 h in CH_4–H_2O: (a) oxidized ZMG232 alloy, (b) oxidized SUS430 alloy.

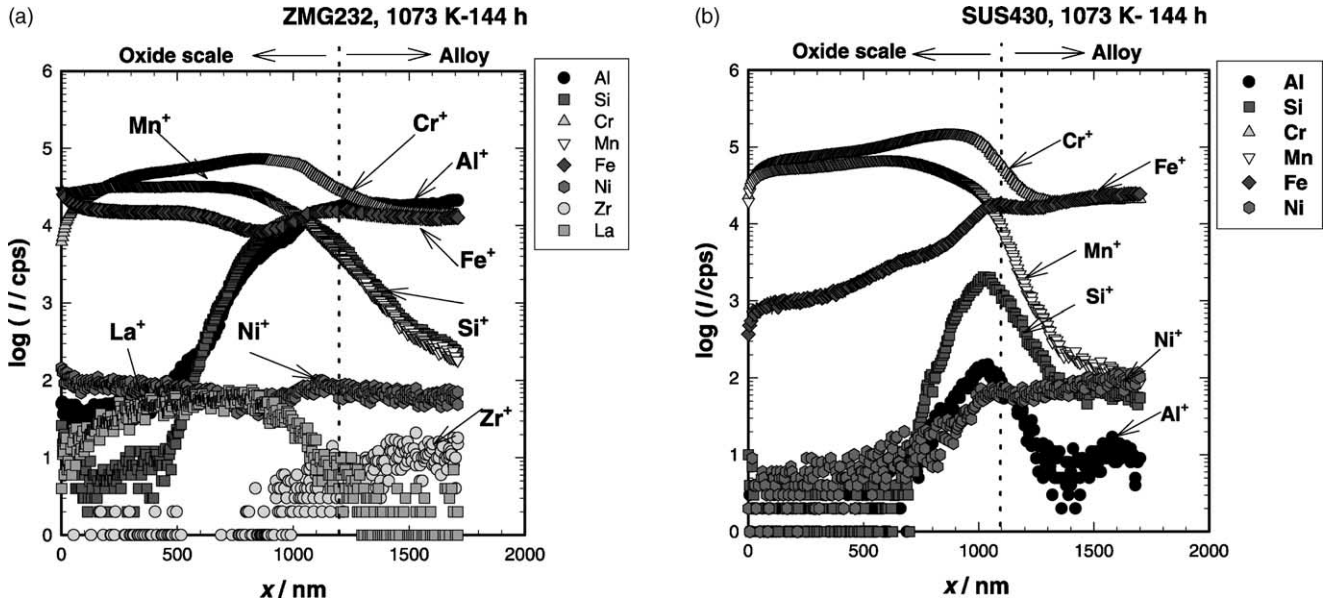

Fig. 7. SIMS depth profiles at the oxide scale/alloy interfaces (oxidation at 1073 K for 144 h in CH_4–H_2O atmosphere): (a) oxidized ZMG232 alloy, (b) oxidized SUS430 alloy.

In Fig. 7b, the distribution of SIMS signal counts is shown around the oxide scale/alloy interface for SUS430. High concentrations of Cr and Mn are observed in the oxide scale. A relatively low Fe-concentration is observed in the oxide scale, and it increases in the alloy. Distinct high concentration profiles of Al and Si are observed at the oxide scale/alloy interface. This indicates the condensation of Al and Si at the oxide scale/alloy interface by annealing in CH_4–H_2O. The profile of Al supports the SEM observation that no inner Al_2O_3 are observed in the SUS430 alloy. The depth profiles of Ni and Al are considerably different between ZMG232 and SUS430. The oxide scale thickness is about 1100 nm from the profile of Cr^+, which is comparable level of ZMG232.

3.4. Oxidation kinetics

The thickness of oxide scale increases with an extension of annealing duration time. The thickness of oxide scale, x, was estimated from SIMS depth profiles of Cr^+ for each sample. Fig. 8 shows growth of oxide scale layer versus annealing duration time. The thickness of oxide scale increase with duration time by the following relationship:

$$x^2 = k_p \times t \quad (1)$$

where k_p is the parabolic growth rate constant, and t is annealing duration time. The solid lines in Fig. 8 are fitting lines of the observed data for each alloy. For both alloys, the growth of oxide scale layer thickness obeys the parabolic law. This implies that the growth of oxide scale is controlled by the diffusion process. From the slopes of the lines, k_p values are calculated for examined two alloys; for SUS430: $k_p = 6.25 \times 10^{-6}$ μm^2/s, and for ZMG232: $k_p = 4.42 \times 10^{-6}$ μm^2/s. The growth rate constants of ZMG232 and SUS430 are similar orders, but SUS430 shows a little bit higher k_p value than ZMG232. This implies that similar growth thicknesses are expected for same annealing duration times.

3.5. SIMS depth profiles of light elements

In CH_4–H_2O fuel gases, the reformed gases or CH_4 are directly contact with alloys, and they may react with alloys

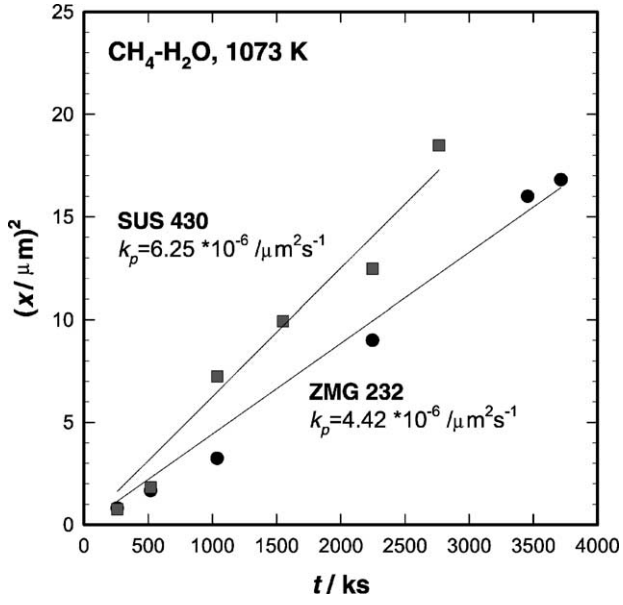

Fig. 8. Growth of oxide scale layers for examined alloys: (●) ZMG232 alloy, (■) SUS430 alloy.

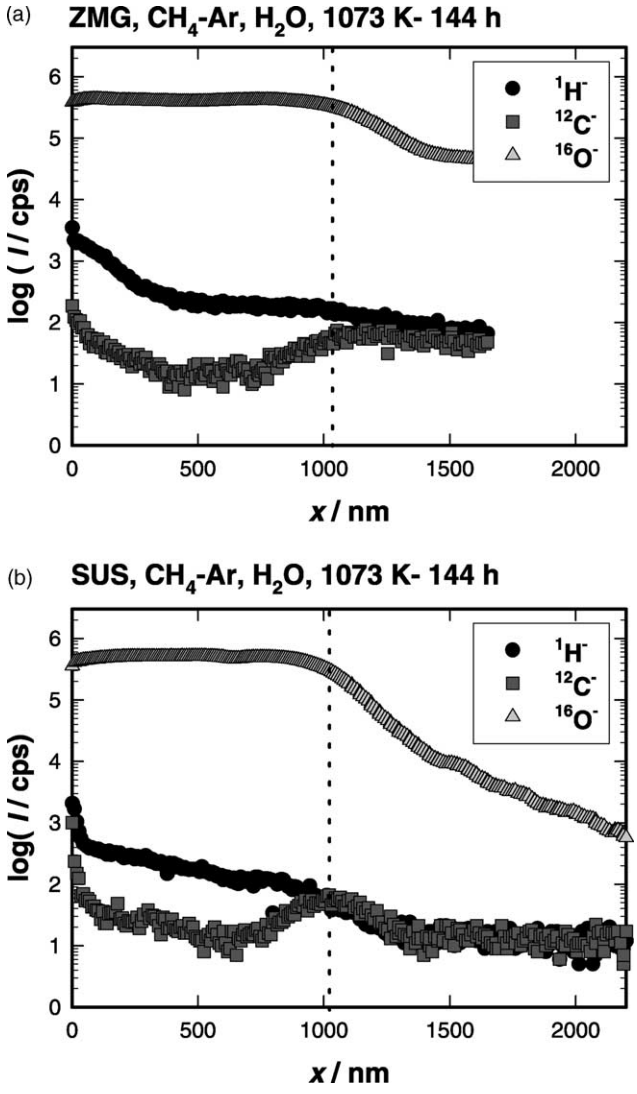

Fig. 9. SIMS depth profiles for light elements (H, C, O) at the oxide scale/alloy interfaces: (a) ZMG232 alloy, (b) SUS430 alloy.

and/or oxide scales. Therefore, the light elements distributions were examined by Cs^+ sputtering of SIMS in the oxide scale. Fig. 9 shows SIMS depth profiles of light elements around the oxide scale/alloy interface. The $^{16}O^-$ profiles show flat part in the surface region that corresponds to the oxide scale on the alloy surface at $x = 0$–1100 nm. Therefore, the oxide scale thickness is thought to be around 1100 nm, which is consistent with the Cr^+ profiles (Fig. 7). Similar $^{16}O^-$ profiles are observed for both ZMG232 and SUS430. Thus, the depths of oxide scales in these two alloys are almost same in this annealing condition.

The $^1H^-$ profiles show gradual decrease of concentration from the surface for both alloys. In the oxidized ZMG, the signal counts of $^1H^-$ decrease to a certain level in the oxide scale. This suggests that H can diffuse into oxide scale from gas phase. On the other hand, the profile of $^1H^-$ in SUS430 shows sudden decrease in the surface region and gradual decrease in the oxide scale. This suggests that the difference

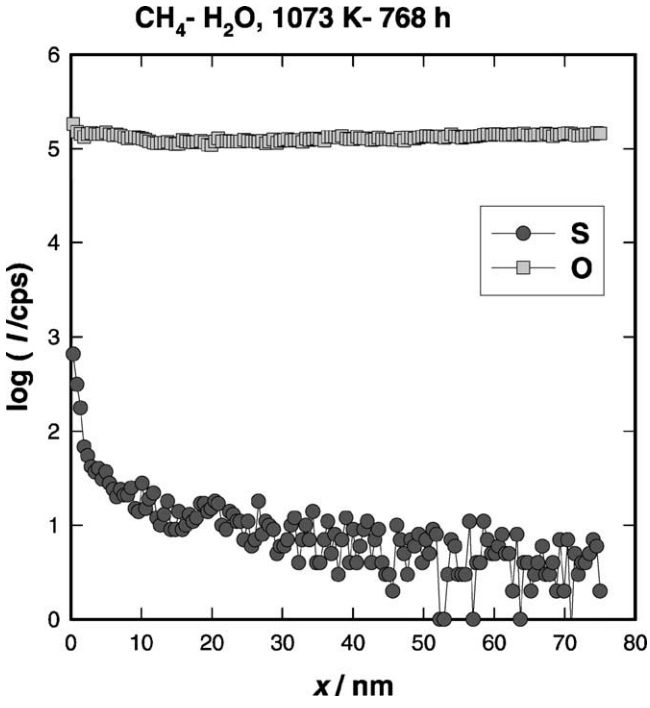

Fig. 10. SIMS depth profiles of sulfur($^{32}S^-$) and oxygen($^{32}O_2^-$) at the oxide scale/ZMG232 alloy interfaces.

of H diffusivity in the formed oxide scale. This may be related to the microstructures of oxide scales.

The depth profiles of $^{12}C^-$ show gradual decrease of signal counts from the oxide scale surface. The maximum of counts are observed around the oxide scale/alloy interface for both alloys. The sources of C are thought to be gas phase or alloy bulk themselves. In the present study, we cannot identify the source of C and exact explanation of these depth profiles in the oxide scale. Further investigation will be made in the future work.

In the CH_4 containing fuels, it may contain a very little amount of sulfur (S) (less than ppm orders) as impurity. Thus, SIMS analysis was conducted for $^{32}S^-$ in a shallow region by the high mass resolution mode ($M/\Delta M = 1000$) to distinguish the mass spectra of $^{32}O^-$ and $^{32}S^-$. Fig. 10 shows SIMS depth profiles of $^{32}O^-$ and $^{32}S^-$ for the oxidized ZMG alloy surface (oxidation in CH_4–H_2O at 1073 K–768 h). The depth profiles of $^{32}S^-$ show a sudden decrease of signal counts from the sample surface. The signal counts of $^{32}S^-$ is background level at deeper than 30 nm. Thus, the diffusion length of S is considered to be only 20–30 nm. S may be diffuse into oxide scale from gas phase from the impurity of CH_4 gas. The amount of S in the oxide scale is considered to be very low, although SIMS analysis is difficult to determine the real concentration.

3.6. Electrical conductivity

Fig. 11 shows electrical conductivity of oxidized alloys as a function of inverse temperature. The electrical

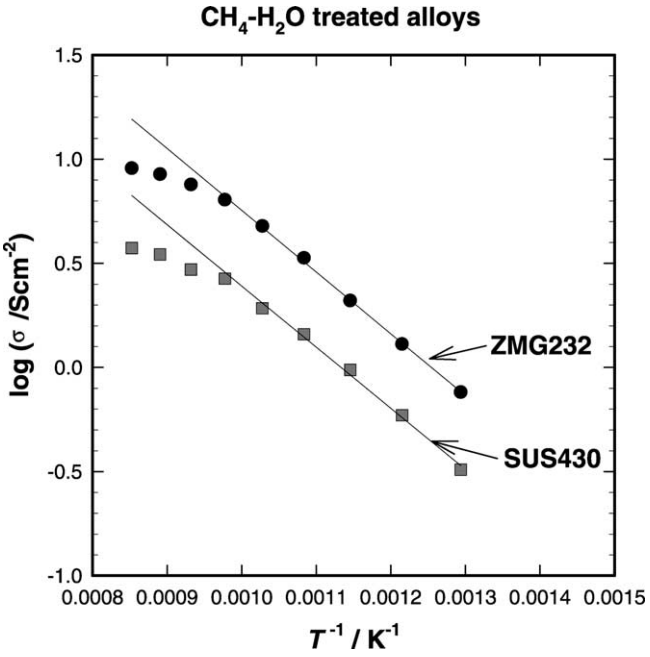

Fig. 11. Electrical conductivity of oxidized alloys: (●) ZMG232 alloy, (■) SUS430 alloy.

conductivity increases with temperature, which suggests the semi-conduction temperature dependence. Therefore, the electrical conductivity mainly shows the contribution from the oxide scales formed on the alloy. For both alloys, the temperature dependence of the conductivity is similar. The activation energy of conductivity is 0.66 eV for ZMG232, and 0.58 eV for SUS430. Similar activation energy indicates that similar conduction mechanism in oxide scale layers. The electrical conductivity of the oxidized ZMG shows higher values than that of the oxidized SUS430. Although the formed phases and oxide scale thickness are similar, the electrical conductivity shows some difference between ZMG232 and SUS430. This may be attributed from the minor element distribution, especially Al and Si distributions around the oxide scale/alloy interfaces. A relatively high Si and Al concentration suggests that insulating layer can be formed at the oxide scale/alloy interface. This insulating layer is more significant in the case of SUS430 to reduce the electrical conductivity.

4. Conclusions

The oxidation behaviors were compared in CH_4–H_2O atmosphere for two kinds of Fe–Cr alloys: SUS430 and ZMG232. Surface microstructure changes and oxide scale layer formation were observed on the oxidized Fe–Cr alloy surface. The main reaction products in the oxide scale were Mn–Cr–Fe spinels and Cr_2O_3 for both alloys. SIMS was applied to measure the elemental distribution of minor and major elements around the oxide scale/alloy interface. A high concentration of Mn on the oxide scale surface suggests that fast diffusion of Mn in the oxide scale to form spinels. Annealing in CH_4–H_2O made the oxide scale thicker with duration time on the alloy surface. Growth of oxide scale layer was evaluated by the parabolic growth relationship. The parabolic growth rate constants for oxide scale were evaluated as follows: $k_p = 6.25 \times 10^{-6}$ μm^2/s for SUS430 and $k_p = 4.42 \times 10^{-6}$ μm^2/s for ZMG232. Similar growth rate values indicated that the thickness of the oxide scale formation was of the same order for both alloys. The electrical conductivity showed semi-conductor temperature dependence for both alloys. The electrical conductivity of oxidized ZMG232 was higher than that of SUS430 in the examined temperature range.

Acknowledgements

The authors are grateful to Dr. Uehara (Hitachi Metals Ltd.) for valuable comments and discussion.

References

[1] W.J. Quadakkers, H. Greiner, W. Köck, in: U. Bossel (Ed.), First European SOFC Forum, The European SOFC Forum, Switzerland, 1994, pp. 525–541.
[2] W. Köck, H. Martinz, H. Greiner, M. Janousek, in: S.C. Singhal, M. Dokiya (Eds.), Solid Oxide Fuel Cell IV, vol. PV95-1, The Electrochemical Society, 1995, pp. 841–849.
[3] H. Greiner, T. Grögler, W. Köck, R.F. Singer, in: S.C. Singhal, M. Dokiya (Eds.), Solid Oxide Fuel Cell IV, vol. PV95-1, The Electrochemical Society, 1995, pp. 879–888.
[4] M. Janousek, W. Köck, M. Baumgärtner, H. Greiner, in: U. Stimming, S.C. Singhal, H. Tagawa, W. Lehnert (Eds.), Solid Oxide Fuel Cells V, vol. PV97-40, The Electrochemical Society, Proceedings Series, Pennington, NJ, USA, 1997, p. 1225.
[5] Th. Malkow, U.v.d. Crone, A.M. Laptev, T. Koppitz, U. Breuer, W.J. Quadakkers, in: U. Stimming, S.C. Singhal, H. Tagawa, W. Lehnert (Eds.), Solid Oxide Fuel Cells V, vol. PV97-40, The Electrochemical Society, Proceedings Series, Pennington, NJ, USA, 1997, p. 1244.
[6] S. Linderoth, P.V. Hendriksen, M. Mogensen, N. Langvad, J. Mater. Sci. 31 (1996) 5077–5082.
[7] W.J. Quadakkers, H. Greiner, M. Hänsel, A. Pattanaik, A.S. Khanna, W. Malléner, Solid State Ionics 91 (1996) 55–67.
[8] S. Lineroth, P.H. Larsen, in: P. Stevens (Ed.), Third European SOFC Forum, 1998, pp. 323–332.
[9] E. Batawi, W. Glatz, W. Kraussler, M. Janousek, B. Doggwiler, R. Diethelm, in: S.C. Singhal, M. Dokiya (Eds.), Solid Oxide Fuel Cells VI, vol. PV99-19, The Electrochemical Society, Proceedings Series, Pennington, NJ, USA, 1999, p. 731.
[10] W. Glatz, E. Batawi, M. Janousek, W. Kraussler, R. Zach, G. Zobal, in: S.C. Singhal, M. Dokiya (Eds.), Solid Oxide Fuel Cells VI, vol. PV99-19, The Electrochemical Society, Proceedings Series, Pennington, NJ, USA, 1999, p. 783.
[11] C. Gindorf, K. Hilpert, L. Singheiser, Solid Oxide Fuel Cells VII, vol. PV2001-16, The Electrochemical Society, Proceedings Series, Pennington, NJ, USA, 2001, p. 793.
[12] K. Honegger, A. Plas, R. Diethelm, W. Glatz, in: S.C. Singhal, H. Yokokawa (Eds.), Solid Oxide Fuel Cells VII, vol. PV2001-16, Pennington, NJ, USA, The Electrochemical Society, 2001, pp. 800–810.
[13] J. Pirmón, Abellán, V. Shemet, F. Tietz, L. Singheiser, W.J. Quadakkers, A. Gil, in: S.C. Singhal, H. Yokokawa (Eds.), Solid

Oxide Fuel Cells VII, vol. PV2001-16, Pennington, NJ, USA, The Electrochemical Society, 2001, pp. 811–819.
[14] O. Teller, W.A. Meulenberg, F. Tietz, E. Wessel, W.J. Quadakkers, in: S.C. Singhal, H. Yokokawa (Eds.), Solid Oxide Fuel Cells VII, vol. PV2001-16, Pennington, NJ, USA, The Electrochemical Society, 2001, pp. 895–903.
[15] T. Brylewski, M. Nanko, T. Maruyama, K. Przybylski, Solid State Ionics 143 (2001) 131–150.
[16] K. Huang, P.Y. Hou, J.B. Goodenough, Solid State Ionics 129 (2000) 237–250.
[17] T. Uehara, T. Ohno, A. Toji, in: J. Huijsmans (Ed.), Proceedings of the 5th European SOFC Forum, European Fuel Cell Forum, 2002, p. 281.
[18] J. Pirón-Abellán, F. Tietz, V. Schemet, A. Gil, T. Ladwein, L. Singheiser, W.J. Quadakkers, in: J. Huijsmans (Ed.), Proceedings of the 5th European SOFC Forum, European Fuel Cell Forum, 2002, p. 248.
[19] T. Horita, Y. Xiong, K. Yamaji, N. Sakai, H. Yokokawa, in: J. Huijsmans (Ed.), Proceedings of the 5th European SOFC Forum, European Fuel Cell Forum, 2002, p. 401.